Symmetric and Asymmetric Decoration of Graphene: Bimetal-Graphene Sandwiches

Peter S. Toth, Matěj Velický, Quentin M. Ramasse, Despoina M. Kepaptsoglou, and Robert A. W. Dryfe**

Low-dimensional carbon materials, i.e., graphene and its functionalization with a number of semiconductor or conductor materials, such as noble metal nanostructures, have primary importance for their potential exploitation as electro-active materials, i.e., as new generation catalysts. Here, low-cost, solution chemistry-based, two-step functionalization of an individual, free-standing, chemical vapor-deposited graphene monolayer is reported, with noble metal (Au, Pt, Pd) nanoparticles to build up two-side decorated graphene-based metal nanoclusters. Either the same metal (symmetric decoration) or different metals (asymmetric decoration) are used for the preparation of bimetal graphene sandwiches, which are adsorbed at the liquid/liquid (organic/water) interface. The successful fabrication of such dual-decorated graphene-based metal nanocomposites is confirmed using various microscopic techniques (scanning electron and atomic force microscopies) and several spectroscopic methods (x-ray photoelectron, energy dispersive x-ray, mapping mode Raman spectroscopy, and electron energy loss spectroscopy). Taken together, it is inferred from these techniques that the location of deposited metal nanoparticles is on opposite sides of the graphene.

1. Introduction

The isolation of a single atom thick, 2D carbon crystal, or graphene (GR), first reported in 2004,[1] initiated an avalanche of research due to the outstanding electronic, optical, and mechanical properties of this material.[2] Graphene synthesis methods have been described extensively, including micromechanical[1] and liquid exfoliation,[3] chemical vapor deposition (CVD),[4] and reduction of graphene-oxide (rGO),[5] all aiming to prepare high-purity, defect-free graphene material with sp^2-bonded carbon atoms in a continuous atomic thick film.

In addition to the synthetic efforts, attempts to functionalize/decorate/dope monolayer GR have also led to a surge of interest in a large number of modification techniques, such as low-cost "wet chemistry"-based doping procedures, to tailor the electronic, structural, and chemical properties of GR.[6] More specifically, the scientific importance of novel gold nanomaterials and carbon nanomaterials has only recently been recognized.[7] This is particularly important as the preparation of metal-decorated carbon supports is a topic of great interest to the catalysis and energy conversion research areas, which has prompted the development of advanced graphene materials for electrochemical energy applications including supercapacitors, batteries, and fuel cells.[8] Asymmetric ("Janus") functionalization tailors the chemical reactivity of the both graphene faces, by altering their topology as well as their electronic structure.[9] The study of double-side functionalized graphene by diazonium molecules[9b] or halogen and phenol groups[9a] showed that "Janus" functionalization is able to significantly increase the reactivity of the opposing graphene face and also produced the highest degree of doping,[9b] and the functionalization on one side is found to be capable of affecting both sides chemical reactivity and physical wettability of the opposite side.[9a] The possibility to prepare novel, asymmetrically decorated graphene structures using "2D chemistry" provides a new aspect to graphene devices and their use as electrode materials.

One issue that has been widely addressed in this context is the extent to which solid substrates, onto which GR is generally transferred, actually dope the graphene layer.[10] There is, on the other hand, a far smaller body of work on the localization of GR (or thicker carbon nanomaterials) at the liquid/liquid interface.[11] Furthermore, the employment of the easily treatable liquid exfoliated GR and rGO flakes to support the deposition of noble metals at organic/water interface has been widely investigated, mainly to prepare graphene-based catalysts or electrode materials on solid substrates.[12] The usage of the CVD GR offers a macroscopic material—visible to the naked eye—that has not been deliberately oxidized, and consists of a high-quality, well-defined monolayer as opposed to liquid-exfoliated GR flakes or rGO aggregates.[11b]

In terms of the electro-catalytic applications of graphene, the determination of kinetic parameters at GR or modified-graphene electrodes is crucial to future development. A significant amount of work has been reported on electrochemistry of mono- and few-layer graphene and investigation of reactivity

Dr. P. S. Toth, Dr. M. Velický, Prof. R. A. W. Dryfe
School of Chemistry
University of Manchester
Oxford Road, M13 9PL Manchester, UK
E-mail: peter.toth@manchester.ac.uk;
robert.dryfe@manchester.ac.uk
Prof. Q. M. Ramasse, Dr. D. M. Kepaptsoglou
SuperSTEM Laboratory
SciTech Daresbury Campus
WA4 4AD Daresbury, UK

DOI: 10.1002/adfm.201500277

of the basal plane and edges/defects, especially to measure the electron transfer kinetics and electro-catalytic activity, for redox active species on different solid substrates[13] and on a free-standing GR film at the interface between two immiscible electrolyte solutions (ITIES).[11a] Electrical polarization of the ITIES generates electrochemical potential gradients capable of promoting ion and electron transfer across the molecular boundary.[14] The nucleation of metallic structures, the catalytic activity of these structures, e.g. with respect to hydrogen and oxygen evolution, and the assembly of nanoparticles or catalytic nanoparticles have all received considerable interest in the last years.[15] A potential, asymmetrically decorated graphene with two distinct metals is of interest due to its potential exploitation as electro-active materials, for example for electro-catalysis at the ITIES, where the two different catalyst materials (e.g., metal NPs) can be used to enhance two different redox reactions (i.e., those occurring in the organic and aqueous phases).

From a characterization point of view, nanoscale, single-molecule structural mapping, in particular using atomic resolution scanning transmission electron microscopy (STEM),[16] and comprehensive molecular-scale property studies have been reported to achieve a detailed understanding of the relationships between structure, properties, and function of the graphene and its decorating nanomaterials.[17] Raman spectroscopy is also a powerful technique to characterize and investigate the chemical modification of CVD GR, as it can detect the presence of covalent bonds, dopants, and their spatial distribution.[18] The Raman spectrum of a single-layer graphene sheet has two characteristic features (G and 2D bands); the G peak is associated with the E_{2g} vibration mode of the sp^2 bonds and the 2D band is caused by the scattering of two phonons and although independent of defects, it is instead affected by strain.[18,19] Both n- and p-type doping of monolayer GR corresponds to a blueshift (frequency increase) of the G band,[20] while the 2D band frequency of single-layer GR increases for p-type doping but decreases for n-type doping. This behavior can be observed in electrochemically gated GR,[19c,20] and by comparison of the relative position and intensity of the G and 2D bands it is relatively easily to determine the degree of doping.[21]

In the present work we develop a very simple, low-cost, solution-based doping technique to tailor the electronic, structural, and chemical properties of graphene, in order to prepare new-generation catalyst materials. CVD GR sheets are either asymmetrically or symmetrically decorated with noble metal nanostructures on both sides of the graphene membrane. This technique is demonstrated here with Au, Pd, and Pt NPs on the top-side and Au or Pd NPs on the underside of GR. Microscopic characterization is then applied to study the nanoscale-structure and morphology of the graphene-based metal nanoclusters. In particular, a combination of atomic force microscopy (AFM), mapping mode Raman spectroscopy, and depth-slicing STEM is used to detect and confirm the location (above or below) of the deposited NPs and nanostructures. Furthermore, high-resolution X-ray photoelectron spectroscopy (XPS) indicates that the deposited Pd on different sides of the CVD GR actually forms oxide nanoclusters rather than pure Pd metal particles.

2. Results

2.1. The Top-Side Decoration of CVD GR Layer

Functionalization of the top of the high-purity CVD GR was achieved by a simple spontaneous redox reaction between the copper foil support underneath the graphene single layer, which acts as an electron donor, and tetrachloroaurate ($AuCl_4^-$) in the aqueous solution (Reaction (1)). The copper surface is oxidized while the Au ions are reduced[22] (see more details in the Experimental Section)

$$AuCl_{4(aq)}^- + 3e^- = Au(s) + 4Cl_{(aq)}^- \quad (1)$$

A schematic of the redox process (**Figure 1**A) and microscopic characterization with images obtained by scanning electron microscopy (SEM) (Figure 1B), AFM (Figure 1C), and STEM (Figure 1D) of the top-side decoration of CVD GR layer by Au NPs (hereafter Au/GR) are shown in Figure 1. The grain boundaries and intrinsic topological defects of graphene are electronically favorable[23] and function as sites with higher activity for deposition.[13c,13f] Previously, we reported that when the bottom side of monolayer CVD GR is decorated with Pd NPs, either spontaneously or electrochemically, the metal NPs are firstly deposited at the topologically higher and electronically favorable grain boundaries, then on the basal planes of graphene.[11b] However, when the CVD GR single layer lies on a copper foil (the substrate for graphene growth) CVD GR follows the surface of the copper, with etches/scratches, so the deposition of Au NPs is also initiated along the etches/scratches on the copper foil, and the electronically favorable intrinsic topological structures, i.e. grain boundaries and edges/defects (Figure S1, Supporting Information). The low magnification SEM image (Figure 1B) shows the full coverage of the Au NPs and nanoflakes/layers on the graphene, however using higher magnification, the AFM image (Figure 1C) depicts line-shaped structures as well, the individual NPs at lower lying planes and the larger nanoflakes/layers of Au are seen all around on the graphene surface. The NP size distribution mainly lies in the range of 5–10 nm, as observed in the high-angle annular dark field (HAADF) STEM image (Figure 1D). More details about the NP nucleation and the different nanoobjects can be found in the Supporting Information (Figure S1).

Given that the same electron donor (copper foil) is used in every case, the thermodynamics of metal deposition on the top of CVD GR are controlled solely by the reduction potentials of any metal species with a higher standard reduction potential than copper ($E^\circ(Cu^{2+}/Cu) = +0.34$ V), which are +1.002, +0.591, and +0.755 V versus standard hydrogen electrode, for the $AuCl_4^-$/Au, $PdCl_4^{2-}$/Pd, and $PtCl_4^{2-}$/Pt couples, respectively.[24] The Pd and Pt NPs size scale was found to be in the 10–20 and 10–50 nm range, respectively. The microscopic characterization of Pd NPs decorated CVD GR (hereafter, Pd/GR) and Pt NPs coated CVD GR (hereafter, Pt/GR) can be seen in Figure S2 (Supporting Information).

The positional shift of the Raman bands (G, 2D) could come either from strain or doping of functionalized graphene, but a simultaneous increase of the position of the G and 2D bands indicates the doping effect of the graphene by the metal

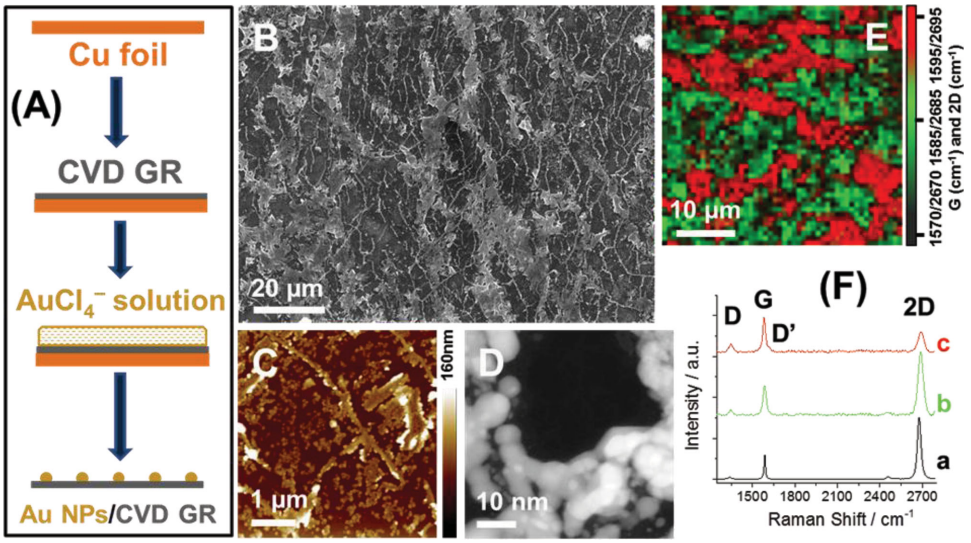

Figure 1. A) Schematic of the $AuCl_4^-$ reduction by Cu foil through CVD GR, resulting in the formation of the "dots" representing Au NPs on the CVD GR layer. B) SEM, C) AFM, and D) STEM images of the Au NPs decorated CVD GR. E) Raman mapping (532 nm excitation laser) of the Au-deposited CVD GR, the different colors depict the change of G and 2D position (most shifted highlighted by red). F) Representative Raman spectra of the Au/GR, each depicts an example from the different areas in (E): a) pristine CVD GR; b) green color marked are; c) red color highlighted area. The Au NPs deposition time was 1 min.

NPs.[9,11b,25] The red and green colored areas on the Raman map (532 nm laser) of the Au/GR (Figure 1E) depict the surface sites where corresponding Raman spectra were recorded (Figure 1F, typical spectra acquired in a given green (b) and red (c) area, compared to the black spectrum, (a) acquired in a region containing pristine CVD GR only). From a visual inspection, the green regions correspond to areas containing smaller and less numerous NPs, while areas covered by larger Au nanoflakes are characterized by a red color. The "green" spectrum (Figure 1F-b), representing the Au NPs decorated areas, shows that the G band is upshifted from 1585.5 cm^{-1} (pristine CVD GR) to 1587.2 cm^{-1}, and the 2D band is upshifted from 2677.1 cm^{-1} (pristine CVD GR) to 2687.3 cm^{-1} and its width is increased from 30.4 cm^{-1} (pristine CVD GR) to 44.5 cm^{-1}. The D (1339.4 cm^{-1}) peak and D' (1618.2 cm^{-1}) shoulder on the G band appeared in the spectra of Au/GR (Figure 1F-b,c), where D corresponds to defective graphene and D' denotes a weak disorder-induced feature.[19a] The same trend in upshift of the G and 2D peaks was observed in the case of the red colored spectrum (Figure 1F-c), corresponding to areas decorated with larger Au nanoflakes. Only two differences between red and green spectra (Figure 1F-c,b) were found. Firstly, there is a decrease of the intensity ratio of the 2D and G bands (I_{2D}/I_G), indicating a higher level of NP functionalization and, secondly, a simultaneous increase of the I_D/I_G demonstrating an increased doping/charging.[9b] Both changes in the intensity ratios demonstrated a higher amount of gold coating on the red colored areas (Figure 1E).

2.2. Preparation of the Bifacial-Decorated CVD GR Layers

The scheme in the top of **Figure 2** illustrates the two steps undertaken to functionalize both sides of the CVD GR, starting with the upper (1st) and followed by the underside (2nd) decoration processes. The 3D schematic on the right best represents the smaller underlying Pd and larger top-deposited Au nanostructures (hereafter, Au/GR/Pd). The process used for the selective deposition of metal NPs onto the underside of CVD GR was described in a recent publication.[11b] SEM (A), SEM-EDAX map (B), and AFM (D) images of the fabricated Au/GR/Pd are presented in Figure 2. Following the scheme of Figure 2, a monolayer sample of CVD GR was first decorated by gold on the top side. The copper foil was then etched from underneath the resultant Au/GR structure, which was then transferred to a $PdCl_4^{2-}$ containing aqueous solution. A 1,2-dichloroethane (DCE) and 5-nonanone mixture in the 1:4 volume ratio was added carefully on the top of the aqueous solution, to allow the organic phase electron donor, decamethylferrocene (DecMFc), to reduce the Pd salt from the underlying aqueous phase via electron transfer through the graphene layer (Reaction (2))

$$PdCl^{2-}_{4(aq)} + 2DecMFc_{(o)} \rightarrow Pd_{(s)} + 4Cl^{-}_{(aq)} + 2DecMFc^{+}_{(o)} \quad (2)$$

The Pd NPs nucleate at the underside of the CVD GR,[11b] thus forming a nanoclustered Au/GR/Pd sandwich. In the case of this bifacial decoration process, the top-side-deposited metal was also employed as a transferring agent, instead of the more conventional polymer film, e.g., polymethyl methacrylate (PMMA). The resultant bifunctionalized Au/GR/Pd was transferred to Si/SiO_2 wafers, or lacey carbon copper grids, to act as substrates for characterization.

Previously, we demonstrated that when both sides of CVD GR single layer are activated at an organic/water interface before the underside deposition occurs (residue free graphene by dissolution of PMMA transferring agent from the top side), the whole underside can be functionalized with smaller Pd NPs, while if some PMMA residues remain on the top side

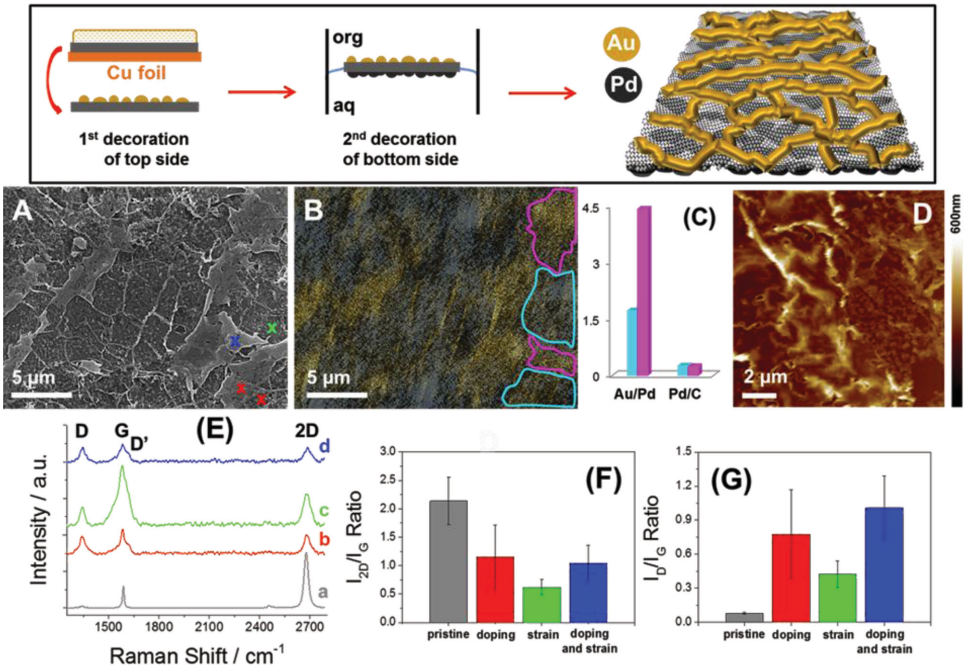

Figure 2. Schemes of the two-side decoration process of graphene with different metal (Au, Pd) NPs (is given on the top of the figure). A) SEM, B) SEM-EDAX map, and C) column graph showing the Au/Pd ratio and the relative Pd metal amount (Pd/C) calculated from the SEM-EDAX map (atomic%), within the areas delimited by magenta and cyan colored lines in (B) and D) AFM image of Au/GR/Pd (panels (A) and (B) show the same area). E) Representative Raman spectra (532 nm excitation laser) of the Au/GR/Pd, each spectrum is a typical example from the different areas that are marked with a cross corresponding to the colors in (A). F,G) Column graphs comparing the Raman peak parameters for dual-decorated and pristine GR layers, with error bars representing the standard deviation. F) The plot of the I_{2D}/I_G and G) I_D/I_G ratios depicts the peak position results of the Au/GR/Pd areas (the Raman spectra highlighted in E). The time of deposition was 1 min in both cases of NPs nucleation, with an organic phase solvent ratio of 1:4 (DCE:5-nonanone) in the case of the underside decoration process (2nd).

during metal deposition, larger Pd NPs nucleate primarily at the grain boundaries rather than basal planes.[11b] In agreement with the correlation between the "both sides activated" CVD GR (i.e., PMMA residue free) and the full covered bottom side of CVD GR by small Pd NPs, the full coverage on the topographically lower parts (bottom side deposited with Pd NPs)—as no PMMA was used for the transfer—and the large Au layers at the top can be clearly seen on Figure 2A–D. The yellow and the gray areas in the SEM-EDAX map of Figure 2B correspond to Au and Pd-rich parts, respectively. Pure gray areas indicate a mostly Pd-rich coating on the underside of CVD GR with no overlayer of Au, while the yellowish areas correspond to a mixture of top-side Au content and full underside coverage with Pd NPs. Examples of the extent of the Au and Pd coatings are schematically represented by magenta and cyan colored lines, respectively. Corresponding elemental ratios (Au/Pd and Pd/C) obtained from the x-ray data from within these highlighted regions are shown on Figure 2C. The extremely similar Pd/C values obtained in the cyan (0.26) and magenta (0.24) prove the full and uniform coverage of the underside of CVD GR by Pd NPs. By contrast, the Au/Pd ratio changes with the presence of large Au layers (ratio of 4.42, within regions delimited by a magenta colored line) or the presence of smaller Au NPs (ratio of 1.72, cyan colored line). Further types of graphene-based nanoclusters can be prepared using either Pt or Pd NPs deposition on the top side and Pd or Au NPs nucleation on the underside, hereafter denoted as Pt/GR/Pd, Pd/GR/Pd, and Pd/GR/Au, respectively.

As shown in Figure 1E,F,G, the doping causes a shift of the peak positions of G and 2D bands and changes the I_{2D}/I_G and I_D/I_G ratios. Due to the electron accepting nature of Au, the graphene is p-doped, leading to a shift in the position of the 2D band toward higher frequencies. This and the intensity ratio changes of the D, G, and 2D bands allow the type and the amount of doping, respectively, to be found, while the change of the full-width at half-maximum of the G peak can be used to distinguish between strain (underside decorated),[25a] doping (either the top or underside functionalization), and doping with strain (dual decoration). The increase of the intensity ratio of D and G bands (I_D/I_G) corresponds to the increase of the doping level of the graphene, so in the case of an asymmetrically functionalized graphene single sheet, the highest I_D/I_G value means when both sides of GR are functionalized.[9b] Figure 2F,G shows each of the peak parameters (I_{2D}/I_G and I_D/I_G ratios) for different regions of the Au/GR/Pd nanocluster, compared for reference to a monolayer CVD GR. Three spectra (Figure 2), color-coded red (b), green (c), and blue (d) were acquired at the positions marked in Figure 2A, and are typical examples of the shifts of G and 2D bands, the width changes of the G band and the changes of the I_D/I_G and I_{2D}/I_G ratios across the Au/GR/Pd samples.

The plot of the I_D/I_G and I_{2D}/I_G ratios (Figure 2G,F) agrees with the peak position results obtained on the Au/GR (Figure 1F) as well as other CVD GR samples for which the top side was decorated by noble metal NPs (Pd/GR and Pt/GR). In all cases, an increased amount of NPs, resulting in the presence

of larger nanoflakes, is accompanied by an increased I_D/I_G ratio, which in turn corresponds to increased doping levels. When the sample was decorated with both Au and Pd to form a bimetal graphene sandwich (blue spectrum, Figure 2E-d), the largest increase in D band intensity was seen, along with the large decrease in 2D intensity (blue columns, Figure 2F,G). The simplest explanation for the observed maximum I_D/I_G value ($I_D/I_G = 1.01 \pm 0.21$) would be the formation of a double-side-decorated CVD GR (comparing to only top-side-decorated graphene, $I_D/I_G = 0.47 \pm 0.07$), i.e. twice the number of available metal NPs attachment sites are occupied, on the top and on the under sides, since both faces of the CVD GR layer are decorated/functionalized. This affects the sp^2 hybridization of the carbon atoms, as in the case reported elsewhere of the covalent bonds due to diazonium-functionalized graphene layers.[9,21] However, this analysis assumes that the initial decoration of the graphene forms on the upper face of the material, rather than depositing between the graphene and the copper substrate to form an alloy or core–shell deposit. Further evidence in favor of the former outcome is presented below.

2.3. Metal and Metal Oxide Formation due to the Decoration

XPS measurements were also performed on metal-decorated CVD GR layers transferred to a Si substrate. The XPS survey spectra are shown in Figures S3 and S4 (Supporting Information). Ten different samples were investigated to compare top-side (Au/GR, Pd/GR, Pt/GR), underside (GR/Pd small, GR/Pd large, GR/Au), and both sides decorated (Au/GR/Pd, Pd/GR/Au, Pt/GR/Pd, Pd/GR/Pd) CVD GR-based nanoclusters. The GR/Pd small (10–40 nm) and GR/Pd large (40–300 nm) nanocomposites deposited on the underside of the monolayer CVD GR are obtained when using two different modes of PMMA (used for transfer only in the case of the underside-decorated samples) dissolution, before, and simultaneously with the Pd NPs deposition, respectively.[11b] The survey spectra are averaged over three different surface sites to obtain maximum sensitivity to trace impurity elements. The quantification was employed using the most intense peaks of the corresponding elements. The peaks used should ideally not overlap with other elements but to achieve the most accurate results, peaks were fitted where there was overlap with either the oxygen 1s orbital (Figure S5A, Supporting Information) or with other metal peaks, e.g. the Pt 4d3/2 peak overlaps with the Pd 3d orbital (Figure S5B, Supporting Information). The full quantification of the spectroscopic data with the corrections across the three different surface sites is found in Tables S1 and S2 (Supporting Information). Analysis of the averaged spectra revealed no substantial variation in the elemental composition. All of the samples contain residual chlorine from the tetrachloro-metal salts or the supporting electrolyte in the case of the underside deposition. **Figure 3**A–D shows the high-resolution XPS spectra of Pd and PdO 3d (A–D), Au 4d5/2 (C, D) orbitals of GR/Pd small (A), Pd/GR/Pd (B), Au/GR/Pd (C), and Pd/GR/Au (D) samples, respectively.

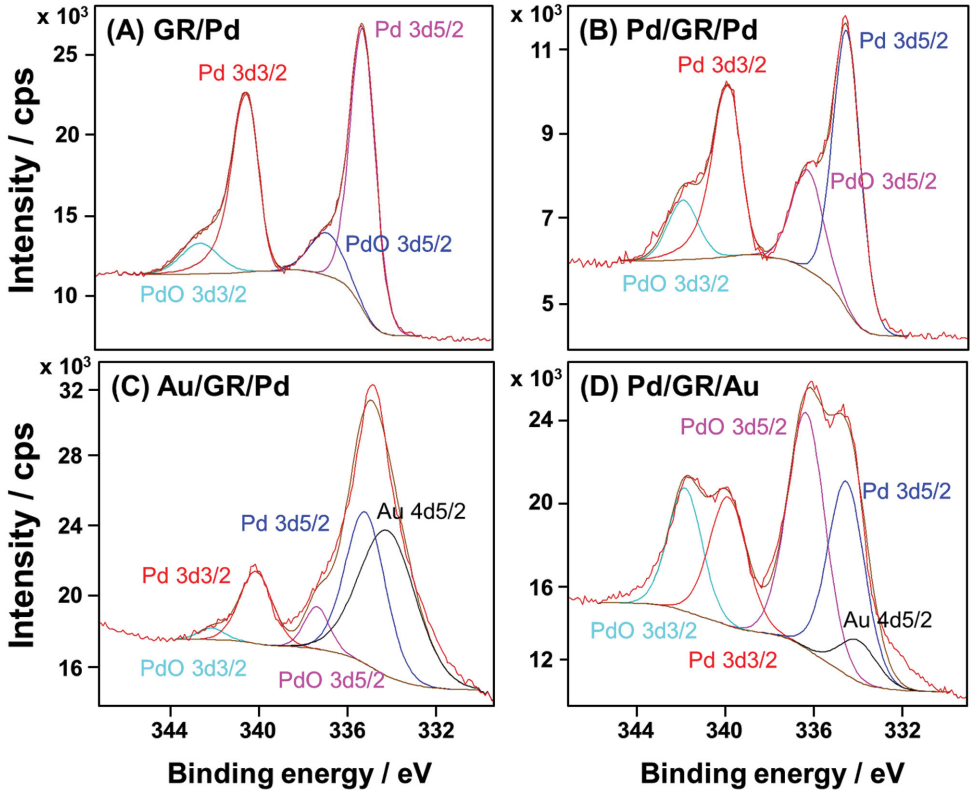

Figure 3. High-resolution X-ray photoelectron spectra of the decorated CVD GR layers: A) GR/Pd, B) Pd/GR/Pd, C) Au/GR/Pd, and D) Pd/GR/Au. All of the spectra show data averaged from three different sites on the surface (spot size of 400 μm^2).

Table 1. The ratio of the zero-valent/metallic (M) and the oxide form (MO) of the metal element (M/MO). The values were calculated from the fittings of the elemental orbitals, the XPS spectra obtained at three different surface sites on the metal NPs decorated CVD GR layers, and the standard deviations are shown in parentheses. The normal and bold fonts correspond to the bottom and top-side-deposited metal content, respectively.

Sample/ratio	Pd/PdO 3d3/2	Pd/PdO 3d5/2	Pt/PtO 4fd5/2	Pt/PtO 4f7/2	Au 4d5/2
Pd/GR	**0.06 (0.01)**	**0.08 (0.01)**	–	–	–
Pt/GR	–	–	**1.63 (0.53)**	**1.57 (0.33)**	–
GR/Pd small	3.32 (1.25)	3.97 (1.26)	–	–	–
Pd/GR/Pd	**2.12 (1.85)**	**1.72 (1.49)**	–	–	–
Pt/GR/Pd	3.00 (1.00)	2.55 (0.93)	**1.36 (0.43)**	**1.56 (0.06)**	–
Au/GR/Pd	7.69 (1.23)	5.73 (0.80)	–	–	**45.64 (7.30)**
Pd/GR/Au	**1.24 (0.22)**	**1.02 (0.28)**	–	–	4.06 (1.73)

The peaks representing the orbitals are split to doublets and some shoulders of the metal elements are found in the high-resolution XPS data. These shoulders correspond to the oxide form of the given metal element except in the case of Au where no oxide was found. The PtO 4f5/2, PtO 4f7/2 were found in lower amounts than the zero-valent element, Pt(0), while the PdO 3d3/2, PdO 3d5/2 content was higher than the Pd(0) (see more in Supporting Information, Figure S6). This can be explained by the nobility of the noble metals, i.e. the standard reduction potential of these oxides.[24] Furthermore, in the case of the underside decoration of CVD GR using Pd NPs, much lower amounts of PdO were observed (Figure 3A–C). **Table 1** shows the ratio of the zero-valent (M) and the oxide form (MO) of the metal element (M/MO) for the compared samples.

The Pd 3d line in the XPS spectrum exhibits two pairs of peaks from the spin-orbital splitting of the 3d3/2 and 3d5/2 (Figure 3A–D) demonstrating the presence of metallic palladium, Pd(0). Moreover two pairs of the PdO shoulders/peaks correspond to the presence of Pd in the 2+ oxidation state along with an overlap with the Au 4d5/2 from the presence of gold or the other side of the sample (Figure 3C,D).

Comparing the top and underside-decorated nanoclusters, specifically the Pd/GR (Figure S6C, Supporting Information) to the GR/Pd small (Figure 3A), respectively, a significant difference can be observed in the amount of Pd oxide detected: 93.47 (±0.98) oxide% (compared to total Pd) is found for Pd/GR compared to an oxide percentage of 22.60 (±4.90) in the case of GR/Pd small (the total Pd atomic percentages are 2.49 and 4.08% as shown in Tables S1 and S2, Supporting Information). A similar trend can also be seen in the case of the symmetrically (Pd/GR/Pd, Figure 3B) and asymmetrically (Au/GR/Pd, Figure 3C and Pd/GR/Au, Figure 3D) functionalized bimetal graphene sandwiches: the M/MO ratio was systematically higher when the Pd metal NPs were nucleated on the underside and lower in the case of the top-side decoration. Comparing the Au/GR/Pd sandwich to its reverse form, Pd/GR/Au, the M/MO ratio for Pd decreases from 7.69 (± 1.23) to 1.24 (± 0.22) (3d3/2) and from 5.73 (± 0.80) to 1.02 (± 0.28) (3d5/2), respectively, while the gold content is also decreased from 45.64 (± 7.30) to 4.06 (± 1.73). A fully quantitative analysis shows similar contents for palladium with, for all the elements, averaged values in an atomic percentage of 2.20 and 2.12 but different amounts of gold with 5.40 and 1.51 at% in the case of Au/GR/Pd and Pd/GR/Au, respectively (see in Supporting Information, Table S1). The specific amount of palladium oxide found in the case of the different decoration processes therefore is an indication of which side of the monolayer CVD GR the metal NPs sit when a dual functionalized graphene sandwich is prepared. Accordingly, the most likely reason for the increase in oxide formation seen for the "top-side"-decorated samples in the sequence Au < Pt < Pd is that the etching of the remaining copper substrate by persulfate used as an etchant (see the Experimental Section) also oxidizes some of the Pt and, in particular, the Pd deposits. It is difficult to avoid this phenomenon, which essentially arises from the similar reduction potentials of the Cu^{2+} ion and the Pd oxide (see values quoted in the Experimental Section).

Morphological and spectroscopic studies can provide structure–property relationships for the carbon-based nanocomposite assemblies, e.g. in the case of the mono-, bi-, and tri-metallic samples on carbon black, or bimetallic palladium–platinum porous nanoballs.[26] The morphology, the size distribution of the metal NPs, and the intensity ratio (XPS) of the different metals in the core–shell configuration can be used to determine, from the order of the sequentially deposited metal NPs, which was deposited first.[15b,26] In order to demonstrate this, a comparison between the individually top-side, bottom-side, and two-sided-decorated CVD GR layers, using Pd and Au metal NPs, was carried out to exclude the formation of core–shell structures on the same side of the graphene single sheet.

The colorful 3D AFM images (in height profile) of the metal NPs decorated CVD GR layers are presented in **Figure 4**: Au/GR (A), GR/Pd small (B), and Au/GR/Pd (C). The full decoration of the underside of graphene by small Pd NPs can be seen for GR/Pd small (B) and Au/GR/Pd (C) via the yellowish color-coded, connected "crumble-like" structures, containing the Pd NPs in the 20–40 nm size range. In the case of the top-side decoration with Au (A), the continuous, green color-coded Au nanolayers can be observed with size distributions (height) mainly lying in the range of 110–130 nm. Using the double-side functionalization process, forming the Au/GR/Pd sandwich structure (C), the topographically higher dark green colored (with purplish color on the top) metal nanoflakes in the 130–190 nm size scale correspond to the underside-deposited Pd NPs (20–40 nm in height) and the top-side-decorated by the Au metal layers (110–130 nm thick). Furthermore, as some parts of the Au/GR/Pd can be seen coated only by the lower Pd NPs (20–40 nm) between the highest structures (130–190 nm) the disparate coverage of the CVD GR layer is indicated.

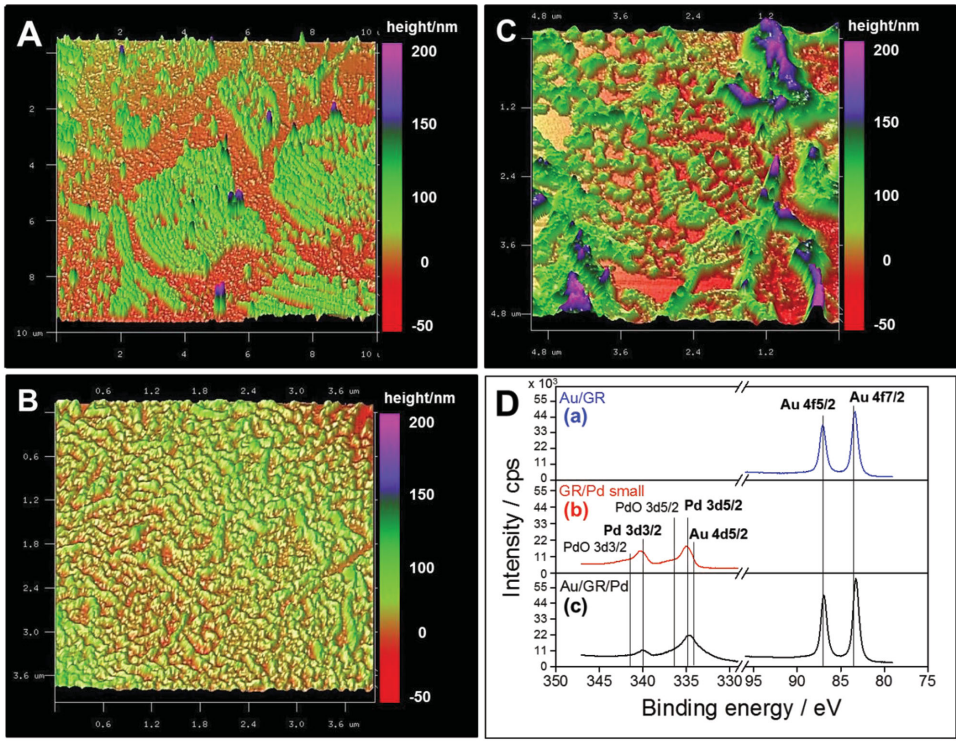

Figure 4. 3D AFM images of the GR-based metal nanoclusters are shown: A) Au/GR, B) GR/Pd small, and C) Au/GR/Pd. D) High-resolution x-ray photoelectron spectra of the decorated CVD GR layers: a) Au/GR, b) GR/Pd small, and c) Au/GR/Pd.

Figure 4D shows the high-resolution XPS spectra of the Pd 3d, PdO 3d, Au 4d5/2 (b, c), and Au 4f (a, c) orbitals of Au/GR (a), GR/Pd small (b), and Au/GR/Pd (c) samples, respectively. The intensity of Au 4f orbitals for the Au/GR (a) and Au/GR/Pd (c) was found to be 40–50 × 10^3 cps and 44–56 × 10^3 cps, respectively. The signal of Pd 3d orbitals for GR/Pd small (b) and Au/GR/Pd (c) was found to be 22–28 × 10^3 cps and 22–32 × 10^3 cps, respectively, so the intensity signals of Au 4f and Pd 3d orbitals are similar for the Au/Gr/Pd sandwich when compared to the case of the only top- (Au/GR) or bottom-side (GR/Pd small) decorated graphene layers. These observations of 3D AFM images and XPS spectra suggest that the both sides of the CVD GR were not uniformly functionalized over the whole surface of the graphene single layer, indicating that the metals were physically distinct from one another, given the known affinity between Au and Pd.

2.4. STEM-EELS Analysis of the Bifacially Decorated CVD GR

HAADF imaging (**Figure 5**A–C) in the STEM reveals the atomic structure of the Au/GR/Pd nanocluster. Figure 5A–C is displayed in false color and with its gamma value adjusted to allow the simultaneous visualization of the heaviest (and therefore very bright) Au nanostructures on the top characterized by the bright yellow aggregates, the moderately heavy Pd NPs in red (and green) (Figure 5A,B), as well as the very light graphene support in blue (Figure 5C). The original (unprocessed) STEM-HAADF images can be found in the Supporting Information (Figure S7).

Further elemental analysis was carried out using electron energy loss spectroscopy (EELS), revealing characteristic spectra of highly graphitic carbon (graphene), gold, and palladium. The HAADF-STEM image in Figure 5D shows a higher magnification of the almost individual structures in the middle part in Figure 5A. EELS spectra are acquired in series at each pixel across the area defined by the green rectangle (Figure 5D) to form a so-called spectrum image. The intensity of the Au $M_{4,5}$ and Pd $M_{4,5}$ edges is then integrated above the corresponding edge onset after subtraction of the background using a power law fit. This yields maps for the localization of Au and Pd across the spectrum image, which can be combined into a composite color map (Figure 5E, where Au is in yellow and Pd is in blue). This map unambiguously confirms the presence of graphene, gold, and palladium particles.[16b] Example spectra of Au and Pd, extracted from the areas dominated by either a yellow or blue color in the map of Figure 5E, are presented in Figure 5F,G. Note that the composite map and spectra are in effect extracted from two data sets acquired consecutively from the very same area, but with different energy ranges to capture all of the C *K* edge, Au $M_{4,5}$ and Pd $M_{4,5}$ edges (the C *K* edge can be seen in Figure S7D, Supporting Information). The EELS data were de-noised using principal component analysis.

The metal content also was characterized by energy dispersive x-ray analysis (EDAX), proving the fabrication of Au/GR/Pd (Figure S10A, Supporting Information) and Pt/GR/Pd (Figure S10B, Supporting Information) sandwiches: this additional characterization is presented in Supporting Information (Figure S10). The applied microscopic techniques (SEM, AFM, and STEM) individually cannot give unambiguous direct

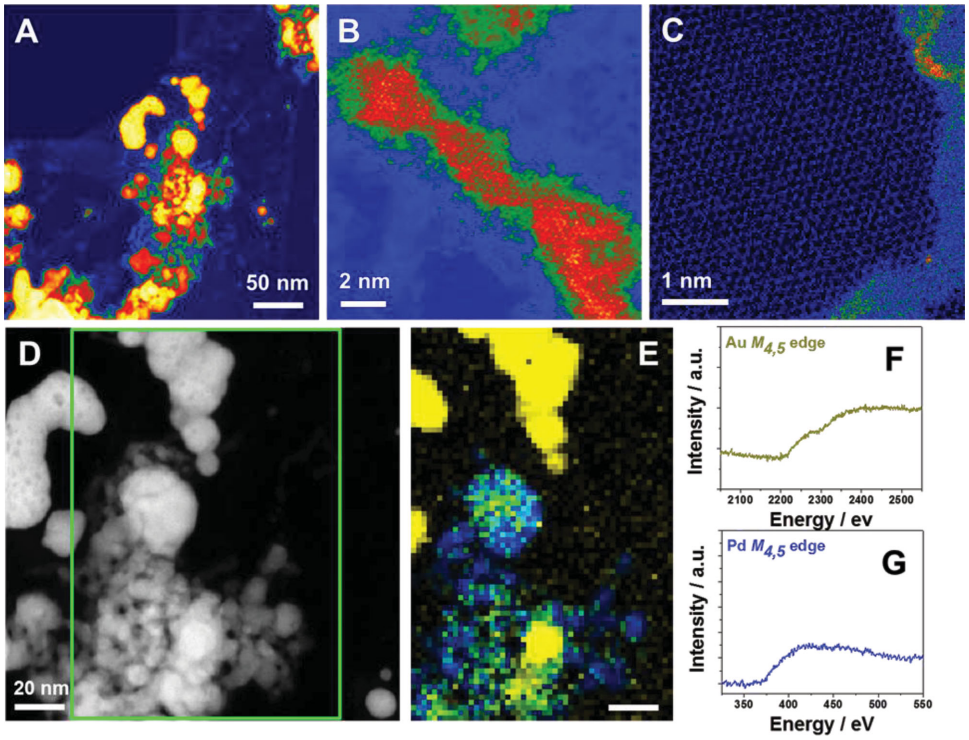

Figure 5. A–C) STEM images of the graphene-based gold (on top) and palladium (underside) decorated nanocluster shown in false color and with the gamma value adjusted to allow the simultaneous visualization of Au (yellow), Pd (red-green), and C (blue) (the relative intensities are therefore not representative of the usual Z-contrast of HAADF images). D) An unprocessed higher magnification HAADF image in the central region of A, with different densities of gray corresponding to Au and Pd levels, with the graphene support hardly visible. E) An EELS chemical map was acquired in the region indicated by a green rectangle in (D): this composite image shows the simultaneous presence of Pd (blue) and Au (yellow). F) Characteristic EELS spectra acquired from a gold-rich (yellow) or G) Pd-rich (blue) zones in (E). F) The clear Au $M_{4,5}$ and G) Pd $M_{4,5}$ signal observed in (E) confirms unambiguously the identification of the particles as Au NPs (yellow) and Pd NPs (blue). Certain regions of the composite color map appear green (in E), corresponding to the presence of both Au and Pd. Carbon from the graphene support is present throughout (not shown), including between the metal particles: dark areas in (E), with an atomic resolution image of the graphene lattice shown in (C). The time of deposition was 1 min in both cases of NPs nucleation with an organic solution volume ratio of 1:4 (DCE:5-nonanone) in the case of the underside decoration process.

evidence for the position/location of the deposited metal NPs relative to the graphene single layer. The combination of the techniques applied here, STEM-EELS mapping, Raman mapping, and high-resolution XPS analysis, provides strong evidence, however. In the STEM-EELS map (Figure 5E), the yellow and blue colors correspond to Au (Au $M_{4,5}$ edge) and Pd (Pd $M_{4,5}$ edge), respectively, while the green colored area demonstrates the presence of a mixture of the two metals. Au and Pd NPs must have therefore nucleated on the distinct sides of the monolayer CVD GR, because otherwise distinct, individual nanostructures would be visible. As can be seen in Figure 5E, both the Au and Pd NPs can be nucleated individually (Au and Pd NPs only on the top side and bottom side of CVD GR, respectively), so individual yellow (Au NPs) and blue (Pd NPs) colored particles are present, while on some parts of the CVD GR, where the green color can be found, the bifacial decoration is visible. This indicates that both sides of the CVD GR were not uniformly functionalized over the whole surface of the graphene membrane. The typical size distribution for the Au and Pd NPs is in the range of the 5–10 and 10–20 nm, respectively. Furthermore, mapping mode Raman spectroscopy shows that, when both sides of CVD GR were decorated with Au on the top and Pd on the bottom to form an asymmetrically decorated graphene bimetal sandwich, the largest increase in D band intensity as well as the large decrease in 2D intensity is observed, affecting the sp^2 hybridization of the carbon atoms (Figure 2). The constructed structures are indeed sandwiches, either metal oxide-graphene-metal sandwich, surprisingly (depending on the side of the deposition), or metal-graphene-metal sandwich. The Au and Pd form very distinct individual nanostructures, which can be distinguished visually, in the STEM-EELS maps the mixtures of Au and Pd are observed in some areas, without any of this individual aspect to the aggregates. Since Au and Pd were deposited at different times and cannot have formed an alloy, then they must have been deposited in different places, and therefore they must be on opposite sides of the graphene sheet.

The correction of optical aberrations up to fifth order in current generation STEM instruments allows the use of very large probe convergence angles (here 31 mrad semi-angle), which means that the depth of field of the images acquired in such probe forming conditions is very shallow (a few nm). This realization has led to the emergence of so-called depth-slicing techniques, which can be used to reveal impurities buried within the sample depth by varying the defocus of the instrument. While for complex optical reasons the depth resolution

is still limited, these techniques can be particularly useful for the observation of interfacial structure at various depths, point defects or spatially limited impurities.[13,27] Here the position of the Au and Pd deposits on top or below a common support graphene layer lends itself to such an approach and a number of through focal series were acquired, having determined the zero focus point as the focus setting for which the sharpest contrast was achieved for the single graphene layer, i.e. the point for which the hexagonal honeycomb pattern of the graphene lattice was observed with maximum contrast (see more details in the Experimental Section, Figures S8 and S9, and Movies S1 and S2, Supporting Information). However, the depth-slicing analysis does suggest that the Au and Pd lie at different depths within the sample, although it is intrinsically difficult to determine the locations from the depth-profiling alone because of the fact that the deposits have different thicknesses. In addition, the applied scanning TEM, EELS chemical mapping, and depth-slicing technique, of course other analytical techniques, in this work are necessary to confirm the sandwich nature of the arrangement.

3. Conclusions

In summary, we have prepared several free-standing CVD GR monolayer-based nanoclusters decorated on both sides with a variety of noble metals using an organic/water interface and two very simple galvanic displacement processes. The top-side decoration was made possible by the copper substrate used for CVD graphene growth, through oxidative etching of the copper coupled with reductive deposition of the noble metal. Small individual metal NPs and larger nanoflakes were detected by microscopy techniques and through changes in positions and intensities of the D, G, and 2D Raman bands. In accordance with the nobility of the top-deposited metal (Au, Pt, and Pd), varying amounts of metal oxides were observed, with more Pd oxide detected than in the case of Pt decoration, while no oxide was observed in the case of Au. The difference in the sample treatments for the top and lower sides of the sample gave different amounts of the Pd oxide on either side of the graphene, allowing us to differentiate between under or top-side Pd NPs deposition. Atomic resolution STEM analysis with HAADF imaging confirmed the presence of the single-layer CVD GR lattice, while the fabrication of an asymmetrically decorated structure was conclusively shown through a combination of microscopic and spectroscopic mapping methods, including STEM-EELS chemical mapping. The decrease of the I_{2D}/I_G and the increase of the I_D/I_G determined from Raman spectroscopy indicated a higher level of functionalization with a higher amount of metal coating.

This work leads to new prospects for graphene modification including the use of in situ Raman spectroscopy to study the in situ deposition/nucleation of NPs on graphene at the organic/water interface, use of the locus between two distinct solution phases to explore mechanisms for potential catalytic processes using modified single-layer graphene, and to achieve the asymmetric functionalization of the monolayer graphene by semiconducting and metallic nanostructures at the polarizable liquid/liquid interface.

4. Experimental Section

Materials: Lithium perchlorate ($LiClO_4$, ≥99.5%), tetrabutyl ammonium perchlorate ($TBAClO_4$, ≥99.0%), ammonium tetrachloropalladate (II) ($(NH_4)_2PdCl_4$, 99.995%), ammonium tetrachloroplatinate (II) ($(NH_4)_2PtCl_4$, 99%), decamethylferrocene or bis(pentamethylcyclopentadienyl) iron(II) ($Me_{10}FeCp_2$, DecMFc, 97%) were purchased from Sigma-Aldrich and hydrogen tetrachloroaurate (III) trihydrate ($HAuCl_4$, 99.99%) was obtained from Alfa Aesar. The residual copper foil under the CVD GR was removed by etching with ammonium persulfate (98%, Lancaster Synthesis Ltd); 3% 950K PMMA in anisole (MicroChem Corp.) was used for graphene transfer only for the underside decoration process (to XPS analysis). The organic phase was formed from mixtures of 1,2-dichloroethane (DCE, ≥99.8%) and di-n-butyl ketone (5-nonanone, 98%) purchased from Sigma-Aldrich and used as received. Deionized water (18.2 MΩ cm resistivity), purified by a "PURELAB" Ultrafiltration unit (Elga Process Water), was used for aqueous solution preparation. Glassware was cleaned in Piranha solution, a 1:4 mixture (by volume) of 30% hydrogen peroxide (H_2O_2, Fisher Scientific) and concentrated sulphuric acid (H_2SO_4, Fisher Scientific)—CAUTION required when handling—boiled in ultrapure water and dried.

CVD Graphene Preparation, the Decoration Processes, and Transfers: The CVD graphene was a gift from the BGT Materials Ltd (Manchester, UK) and was prepared using methods previously reported.[4] Three kinds of functionalization of the graphene layers were carried out: top-side, underside, and two-sided (bifacial) decoration. The top-side decoration of the CVD GR was performed using a simple galvanic displacement reaction for the nucleation of metal NPs (Au, Pd, and Pt), using the copper foil, which acts as an electron donor under the graphene monolayer, and transfers electrons to the noble metal.[22] The metal-decorated CVD GR layers on the copper foil were washed to remove the unreacted metal salts ($AuCl_4^-$, $PdCl_4^{2-}$, and $PtCl_4^{2-}$) and blow-dried with nitrogen. The Au/GR/copper, Pd/GR/copper, and Pt/GR/copper stacks thus obtained were subsequently treated to remove the residual copper foil through etching in 0.5 M ammonium persulfate solution. Then the resulting Au/GR, Pd/GR, and Pt/GR layers were cleaned three times by transfer to pure water, prior to fishing out the layers with a solid substrate, dried in air for 15 min, then washed in an ethanol and isopropanol mixture (5 min), followed by acetone (5 min), and finally blow-dried with nitrogen. Considering the Pourbaix diagrams and the standard reduction potentials of Au, Pd, and Pt,[24,28] the potential of the metal oxides formation from the metals is increasing in the sequence Pd (≈ +0.4 V), Pt (≈ +0.6 V), and Au (≈ +0.9 V) at pH ≈ 9, as the $(NH_4)_2PdCl_4$, $(NH_4)_2PtCl_4$ and $HAuCl_4$, aqueous solutions pH values are in the 8–10 range. Therefore during the nucleation of the zero-valent/metallic (M) particles on the CVD GR (on the underlying copper foil) with a higher standard reduction potential than copper ($E^\circ(Cu^{2+}/Cu) = +0.34$ V), which are +0.591, +0.755, and +1.002 V versus standard hydrogen electrode, for the $PdCl_4^{2-}$/Pd, $PtCl_4^{2-}$/Pt, and $AuCl_4^-$/Au couples, respectively, the oxide form of the metals (MO) can be formed immediately on the lower potential and higher pH values. Another simple, spontaneous metal (Au, Pd) deposition was applied at the interface-assembled CVD GR to decorate the underside of graphene, thus creating GR/Au and GR/Pd layers. This functionalization and transfer process has been described in previous work.[11b] Briefly, the interface-assembled high-purity CVD GR was decorated by an interfacial redox reaction between DecMFc, which is the organic phase electron donor, and aqueous metal salts ($PdCl_4^{2-}$, $AuCl_4^-$). This metal NP deposition can proceed spontaneously at the liquid/liquid interface,[29] but in the presence of the graphene layer, it is found to occur preferentially on the graphene.[11b] The combination of these two methods (top and bottom-side decoration) was applied to obtain a symmetric and asymmetric functionalization of the graphene layer, to prepare the bifacially decorated monolayer graphene with metal NPs of the same or distinct metals. More details of the decorated CVD GR layers transfer are given in the Supporting Information.

Decorated Graphene Characterization: Raman analysis was carried out using a Renishaw RM 264N94 (532 nm laser) spectrometer operating at power ≤1 mW. The SEM (Philips XL30 ESEM-FEG, operated at 15 kV),

the AFM (Bruker MultiMode 8, operated in "Peak Force" tapping mode with a silicon tip on a silicon nitride lever) characterization was performed on the samples once transferred to a Si/SiO_2 wafer. Further characterization was carried out by STEM (Nion Ultrastem™ 100, SuperSTEM), using specifically prepared free-standing samples supported on lacey carbon-coated copper grids (TAAB Laboratories Equipment Ltd). Elemental analysis of the decorated CVD GR layers was obtained using XPS, EDAX, and EELS techniques at three to five different surface sites. XPS analysis was performed using the largest available spot size (400 μm^2) on K-Alpha monochromated (Al–1486 eV) X-ray Photoelectron Spectrometer system (Thermo Fisher Scientific, Inc). All XPS data were analyzed and quantified using CasaXPS Software (version 2.3.16, www.casaxps.com). The EDAX spectrometer was attached to the SEM and operated at 15 kV for the elemental analysis. EELS spectra were recorded using a Gatan Enfina spectrometer, with a collection semi-angle of 37 mrad. More details of the STEM instrumentation are given in the Supporting Information.

Supporting Information

Supporting Information is available from the Wiley Online Library or from the author.

Acknowledgements

The authors thank the UK EPSRC (Grant Nos. EP/K007033/1, EP/K039547/1, and EP/K016954/1) for financial support. The authors also thank NEXUS at nanoLAB (Newcastle University) for XPS measurements. SuperSTEM is the EPSRC National Facility for Aberration-Corrected Scanning Transmission Electron Microscopy. The first name of author D.M.K. was corrected on May 20, 2015.

Received: January 22, 2015
Revised: February 27, 2015
Published online: March 30, 2015

[1] K. S. Novoselov, A. K. Geim, S. V. Morozov, D. Jiang, Y. Zhang, S. V. Dubonos, I. V. Grigorieva, A. A. Firsov, *Science* **2004**, *306*, 666.

[2] a) I. Vlassiouk, S. Smirnov, I. Ivanov, P. F. Fulvio, S. Dai, H. Meyer, M. Chi, D. Hensley, P. Datskos, N. V. Lavrik, *Nanotechnology* **2011**, *22*,9; b) C. M. Weber, D. M. Eisele, J. P. Rabe, Y. Liang, X. Feng, L. Zhi, K. Mullen, J. L. Lyon, R. Williams, D. A. Vanden Bout, K. J. Stevenson, *Small* **2010**, *6*, 184; c) K. S. Novoselov, A. K. Geim, S. V. Morozov, D. Jiang, M. I. Katsnelson, I. V. Grigorieva, S. V. Dubonos, A. A. Firsov, *Nature* **2005**, *438*, 197.

[3] Y. Hernandez, V. Nicolosi, M. Lotya, F. M. Blighe, Z. Sun, S. De, I. T. McGovern, B. Holland, M. Byrne, Y. K. Gun'ko, J. J. Boland, P. Niraj, G. Duesberg, S. Krishnamurthy, R. Goodhue, J. Hutchison, V. Scardaci, A. C. Ferrari, J. N. Coleman, *Nat. Nanotechnol.* **2008**, *3*, 563.

[4] X. Li, W. Cai, J. An, S. Kim, J. Nah, D. Yang, R. Piner, A. Velamakanni, I. Jung, E. Tutuc, S. K. Banerjee, L. Colombo, R. S. Ruoff, *Science* **2009**, *324*, 1312.

[5] H. L. Poh, F. Sanek, A. Ambrosi, G. Zhao, Z. Sofer, M. Pumera, *Nanoscale* **2012**, *4*, 3515.

[6] a) J. A. Robinson, M. Hollander, M. LaBella, K. A. Trumbull, R. Cavalero, D. W. Snyder, *Nano Lett.* **2011**, *11*, 3875; b) A. Mishchenko, J. S. Tu, Y. Cao, R. V. Gorbachev, J. R. Wallbank, M. T. Greenaway, V. E. Morozov, S. V. Morozov, M. J. Zhu, S. L. Wong, F. Withers, C. R. Woods, Y.-J. Kim, K. Watanabe, T. Taniguchi, E. E. Vdovin, O. Makarovsky, T. M. Fromhold, V. I. Fal'ko, A. K. Geim, L. Eaves, K. S. Novoselov, *Nat. Nanotechnol.* **2014**, *9*, 808.

[7] G. Y. Vélez, A. Encinas, M. Quintana, *Functionalization of Graphene*, Wiley-VCH, Weinheim, Germany **2014**.

[8] a) V. H. Rodrigues de Souza, M. M. Oliveira, A. J. Gorgatti Zarbin, *J. Power Sources* **2014**, *260*, 34; b) P. V. Kamat, *J. Phys. Chem. Lett.* **2010**, *1*, 520; c) J. M. Yuk, K. Kim, B. n. Alemán, W. Regan, J. H. Ryu, J. Park, P. Ercius, H. M. Lee, A. P. Alivisatos, M. F. Crommie, J. Y. Lee, A. Zettl, *Nano Lett.* **2011**, *11*, 3290.

[9] a) L. Zhang, J. Yu, M. Yang, Q. Xie, H. Peng, Z. Liu, *Nat. Commun.* **2013**, *4*, 1443; b) M. A. Bissett, Y. Takesaki, M. Tsuji, H. Ago, *RSC Adv.* **2014**, *4*, 52215.

[10] a) V. D. Dao, L. V. Nang, E. T. Kim, J. K. Lee, H. S. Choi, *ChemSusChem* **2013**, *6*, 1316; b) S. A. You, O. S. Kwon, J. Jang, *J. Mater. Chem.* **2012**, *22*, 17805.

[11] a) P. S. Toth, A. N. J. Rodgers, A. K. Rabiu, R. A. W. Dryfe, *Electrochem. Commun.* **2015**, *50*, 6; b) P. S. Toth, Q. M. Ramasse, M. Velicky, R. A. W. Dryfe, *Chem. Sci.* **2015**, *6*, 1316.

[12] a) S. J. Hoseini, M. Dehghani, H. Nasrabadi, *Catal. Sci. Technol.* **2014**, *4*, 1078; b) K. Bramhaiah, N. S. John, *RSC Adv.* **2013**, *3*, 7765; c) X. Zan, Z. Fang, J. Wu, F. Xiao, F. Huo, H. Duan, *Biosens. Bioelectron.* **2013**, *49*, 71; d) M. M. Gudarzi, F. Sharif, *Soft Matter* **2011**, *7*, 3432; e) S. Biswas, L. T. Drzal, *Nano Lett.* **2009**, *9*, 167; f) R. V. Salvatierra, S. H. Domingues, M. M. Oliveira, A. J. G. Zarbin, *Carbon* **2013**, *57*, 410.

[13] a) A. G. Gueell, N. Ebejer, M. E. Snowden, J. V. Macpherson, P. R. Unwin, *J. Am. Chem. Soc.* **2012**, *134*, 7258; b) C. B. Ekanayake, M. B. Wijesinghe, C. G. Zoski, *Anal. Chem.* **2013**, *85*, 4022; c) P. S. Toth, A. T. Valota, M. Velický, I. A. Kinloch, K. S. Novoselov, E. W. Hill, R. A. W. Dryfe, *Chem. Sci.* **2014**, *5*, 582; d) M. Velický, D. F. Bradley, A. J. Cooper, E. W. Hill, I. A. Kinloch, A. Mishchenko, K. S. Novoselov, H. V. Patten, P. S. Toth, A. T. Valota, S. D. Worrall, R. A. W. Dryfe, *ACS Nano* **2014**, *8*, 10089; e) S. H. Oh, K. v. Benthem, S. I. Molina, A. Y. Borisevich, W. Luo, P. Werner, N. D. Zakharov, D. Kumar, S. T. Pantelides, S. J. Pennycook, *Nano Lett.* **2008**, *8*, 1016; f) A. Shen, Y. Zou, Q. Wang, R. A. W. Dryfe, X. Huang, S. Dou, L. Dai, S. Wang, *Angew. Chem. Int. Ed.* **2014**, *53*, 10804.

[14] Z. Samec, *Pure Appl. Chem.* **2004**, *76*, 2147.

[15] a) H. Jensen, D. J. Fermin, J. E. Moser, H. H. Girault, *J. Phys. Chem. B* **2002**, *106*, 10908; b) X. Liu, E. H. Yu, K. Scott, *Appl. Catal. B* **2015**, *162*, 593; c) H. Deng, T. J. Stockmann, P. Peljo, M. Opallo, H. H. Girault, *J. Electroanal. Chem.* **2014**, *731*, 28.

[16] a) R. Zan, Q. M. Ramasse, U. Bangert, K. S. Novoselov, *Nano Lett.* **2012**, *12*, 3936; b) Q. M. Ramasse, R. Zan, U. Bangert, D. W. Boukhvalov, Y.-W. Son, K. S. Novoselov, *ACS Nano* **2012**, *6*, 4063.

[17] a) Y. Wu, W. Jiang, Y. Ren, W. Cai, W. H. Lee, H. Li, R. D. Piner, C. W. Pope, Y. Hao, H. Ji, J. Kang, R. S. Ruoff, *Small* **2012**, *8*, 3129; b) V. B. Parambhath, R. Nagar, S. Ramaprabhu, *Langmuir* **2012**, *28*, 7826; c) P. A. Pandey, G. R. Bell, J. P. Rourke, A. M. Sanchez, M. D. Elkin, B. J. Hickey, N. R. Wilson, *Small* **2011**, *7*, 3202; d) W. Pierce, R. Zan, Q. M. Ramasse, C. B. Boothroydand, U. Bangert, *J. Phys. Conf. Ser.* **2014**, *522*, 4; e) K. Kim, H.-B.-R. Lee, R. W. Johnson, J. T. Tanskanen, N. Liu, M.-G. Kim, C. Pang, C. Ahn, S. F. Bent, Z. Bao, *Nat. Commun.* **2014**, *5*, 4781.

[18] A. C. Ferrari, D. M. Basko, *Nat. Nanotechnol.* **2013**, *8*, 235.

[19] a) A. C. Ferrari, J. C. Meyer, V. Scardaci, C. Casiraghi, M. Lazzeri, F. Mauri, S. Piscanec, D. Jiang, K. S. Novoselov, S. Roth, A. K. Geim, *Phys. Rev. Lett.* **2006**, *97*,187401; b) O. Frank, G. Tsoukleri, J. Parthenios, K. Papagelis, I. Riaz, R. Jalil, K. S. Novoselov, C. Galiotis, *ACS Nano* **2010**, *4*, 3131; c) M. Kalbac, H. Farhat, J. Kong, P. Janda, L. Kavan, M. S. Dresselhaus, *Nano Lett.* **2011**, *11*, 1957; d) Z. Komínková, M. Kalbáč, *Phys. Status Solidi B* **2013**, *250*, 2659; e) Z. V. Živcová, O. Frank, V. Petrák, H. Tarábková, J. Vacík, M. Nesládek, L. Kavan, *Electrochim. Acta* **2013**, *87*, 518.

[20] A. Das, B. Chakraborty, S. Piscanec, S. Pisana, A. K. Sood, A. C. Ferrari, *Phys. Rev. B* **2009**, *79*, 155417.
[21] a) M. A. Bissett, M. Tsuji, H. Ago, *J. Phys. Chem. C* **2013**, *117*, 3152; b) M. A. Bissett, S. Konabe, S. Okada, M. Tsuji, H. Ago, *ACS Nano* **2013**, *7*, 10335.
[22] A. Gutes, B. Hsia, A. Sussman, W. Mickelson, A. Zettl, C. Carraro, R. Maboudian, *Nanoscale* **2012**, *4*, 438.
[23] a) O. V. Yazyev, S. G. Louie, *Phys. Rev. B* **2010**, *81*, 195420; b) A. Ayuela, W. Jaskólski, H. Santos, C. Leonor, *New J. Phys.* **2014**, *16*, 083018.
[24] a) S. G. Bratsch, *J. Phys. Chem. Ref. Data* **1989**, *18*, 1; b) A. J. Bard, R. Parsons, J. Jordan, *Standard Potentials in Aqueous Solutions*, Marcel Dekker, NY **1985**.
[25] a) M. W. Iqbal, A. K. Singh, M. Z. Iqbal, J. Eom, *J. Phys. Condens. Matter* **2012**, *24*, 335301; b) D. Yu, E. Nagelli, R. Naik, L. Dai, *Angew. Chem. Int. Ed.* **2011**, *50*, 6575.
[26] a) K. Rajeshwar, C. Janaky, W. Y. Lin, D. A. Roberts, W. Wampler, *J. Phys. Chem. Lett.* **2013**, *4*, 3468; b) A. Lehoux, L. Ramos, P. Beaunier, D. B. Uribe, P. Dieudonné, F. Audonnet, A. Etcheberry, M. José-Yacaman, H. Remita, *Adv. Funct. Mater.* **2012**, *22*, 4900.
[27] a) E. C. Cosgriff, P. D. Nellist, *Ultramicroscopy* **2007**, *107*, 626; b) K. van Benthem, A. R. Lupini, M. P. Oxley, S. D. Findlay, L. J. Allen, S. J. Pennycook, *Ultramicroscopy* **2006**, *106*, 1062; c) J. E. Allen, E. R. Hemesath, D. E. Perea, J. L. Lensch-Falk, Z.Y Li, F. Yin, M. H. Gass, P. Wang, A. L. Bleloch, R. E. Palmer, L. J. Lauhon, *Nat. Nanotechnol.* **2008**, *3*, 168; d) C. Kisielowski, B. Freitag, M. Bischoff, H. van Lin, S. Lazar, G. Knippels, P. Tiemeijer, M. van der Stam, S. von Harrach, M. Stekelenburg, M. Haider, S. Uhlemann, H. Müller, P. Hartel, B. Kabius, D. Miller, I. Petrov, E. A. Olson, T. Donchev, E. A. Kenik, A. R. Lupini, J. Bentley, S. J. Pennycook, I. M. Anderson, A. M. Minor, A. K. Schmid, T. Duden, V. Radmilovic, Q. M. Ramasse, M. Watanabe, R. Erni, E. A. Stach, P. Denes, U. Dahmen, *Microsc. Microanal.* **2008**, *14*, 469.
[28] a) M. Pourbaix, *Atlas of Electrochemical Equilibria in Aqueous Solutions*, National Association of Corrosion Engineers, Houston, TX, USA **1974**; b) E. McCafferty, *Introduction to Corrosion Science*, Springer, New York, NY, USA **2010**.
[29] R. A. W. Dryfe, A. O. Simm, B. Kralj, *J. Am. Chem. Soc.* **2003**, *125*, 13014.